Experimental investigation on nanowire array irradiated with ultrahigh intensity laser at X-ray free electron laser facility SACLA: Fabrication of nanowire array target and its application to ultrafast time-resolved measurements

*D. Tanaka[1)], H. Sawada[2)], T. Idesaka[1)], C. Nakatsuji[1)], S. Matsuura[1)],
T.Sato[1)], T. Somekawa[3)], T. Yabuuchi[4,5)], K. Miyanishi[5)], K. Sueda[5)], Y.Inubushi[4,5)],
Y.Sentoku[1)], T. Shimizu[6)], S. Shingubara[6)], K. Kawasaki[1)], N.Ozaki[7)], K. Yamanoi[1)]
and K. Shigemori[1)]

[1)]Institute of Laser Engineering, Osaka University
2-6 Yamada-oka, Suita, Osaka, 565-0871, Japan
[2)] University of Nevada Reno, Reno, NV, 89557, USA,
[3)] Institute for Laser Technology
2-6 Yamada-oka, Suita, Osaka 565-0871, Japan
[4)] Japan Synchrotron Radiation Research Institute,
1-1-1 Kouto, Sayo-cho, Sayo-gun, Hyogo 679-5148, Japan
[5)] RIKEN SPring-8 Center,
1-1-1 Kouto, Sayo-cho, Sayo-gun, Hyogo 679-5148, Japan
[6)] Graduate School of Science and Engineering, Kansai University,
3-3-35 Yamate-cho, Suita, Osaka 564-8680, Japan
[7)] Graduate School of Engineering, Osaka University,
2-1 Yamada-oka, Suita, Osaka 565-0871, Japan

E-mail: u308634c@ecs.osaka-u.ac.jp
*Corresponding author: Daisuke Tanaka (e-mail: u308634c@ecs.osaka-u.ac.jp)

Abstract

Nanowire arrays—vertically aligned metal wires with a few hundred nanometers in diameter—are promising nano-structured targets for high-energy-density physics and related applications. We have been developing an ultrafast, time-resolved measurements on laser-irradiated targets using the x-ray free electron laser at the SACLA facility. Here, we present fabrication of various kinds of nanowire array in order to explore the absorption mechanism with ultrahigh intensity laser irradiation, and their application to the laser

irradiation experiment performed at the SACLA facility. To fabricate nanowire arrays with control over their spatial and material parameters, we have developed an approach using an anodic aluminum oxide (AAO) template and electroplating processes. The nanowire array samples were applied for ultrahigh intensity laser experiments, which coupled with x-ray free-electron-laser facility SACLA. We characterized fundamental "static" data on transmittance calibration for x-ray shadowgraph measurements. We also evaluated effect of pre-pulse on spatial changes of nanowire, showing that the shape of the nanowires was maintained up to a few picoseconds after laser irradiation. On the preliminary laser-irradiation experiments, we observed time-resolved, two-dimensional x-ray images and observed the x-ray transmittance change due to heating process.

1. Introduction

The emergence of chirped-pulse amplification[1] in the 1990s has enabled the peak intensity of short laser pulses to be increased dramatically, reaching the relativistic regime (over ~1.0 × 10^{18} W/cm^2). The resulting ultra-intense laser–matter interactions have led to the development of various applications, such as fast-ignition inertial-confinement fusion[2–4] , electron[5-9] and ion acceleration[10-12], neutron generation[13-15], and x-ray emission[16-18]. In general, an ultra-intense short-pulse laser has a pre-pulse, which is a low-intensity laser pulse that precedes the main peak of the laser light[19-21]. This pre-pulse ionizes the solid target and creates a low-dense plasma called a "pre-plasma." The main laser pulse then cannot interact with the target surface because it is reflected by the overdense plasma layer in the pre-plasma, and the absorption of laser energy therefore remains low. To overcome this problem, many research groups have proposed using structured targets, which have nano- or micro-sized artificial structures on their surfaces. Many kinds of targets have been suggested to date, including gratings[22,23], nanotubes[24], nano- or micro-sized spheres[25,26], and foam targets[27,28].

In this context, nano- or microwire arrays—in which micro-scale wires are aligned perpendicular to the substrate surface—have recently attracted much attention[29-43]. In a nanowire array, laser energy is absorbed efficiently because the laser light penetrates the gaps between the nanowires to a depth of a few micrometers[30], enabling the creation of larger volumes of hot, dense matter (i.e., states of ultrahigh energy density) in laser-irradiated nanowire arrays than in those obtained from typical flat foils. For example, Purvis et al. utilized an ultrahigh contrast intense laser to generate states of ultrahigh energy density (i.e., with pressures exceeding a Gbar) with a laser energy of 0.5 J[30]. In addition, Bargsten et al. used experiments and numerical simulations to show that a volumetric plasma with a length scale of a few μm can be created in a nanowire array[31]. Many research groups have focused on the high absorption of laser energy by nanowire arrays, and various applications have been investigated, including beam nuclear fusion[32-34], particle acceleration[35,36], and high-brilliance x-ray sources[37,38].

To explore such applications, it is crucial to investigate how the laser energy is absorbed and transported in a nanowire array. The geometry of the nanowire array (e.g., the nanowire diameter, nanowire length, filling factor, and arrangement of the nanowires) is expected to affect the energy absorption strongly. Many research groups have therefore focused on the effect of the geometry of the nanowire array on laser energy absorption[39-41]. Park et al. showed that the reflection of laser light is suppressed as the area interacting with the laser is increased[39]. Cristoforetti et al. pointed out that large-spaced nanowire arrays are suitable for particle acceleration, while—due to stochastic heating—smaller-spaced wires are more suitable for generating high-energy-density states[40]. In addition, our previous study showed that strong magnetic fields are generated around periodically arrayed nanowires during laser irradiation[41]. This intense magnetic field traps hot electrons and improves the absorption of laser energy by the nanowire array. The geometry of a nanowire array is therefore critical when considering its interaction with laser-irradiation.

However, previous studies only compared the time-integrated experimental measurements with the results of numerical simulations. Few investigations observed the temporal evolution in a nanowire array irradiated by an ultrahigh intensity laser beam[42,43] because the duration of the laser pulse is too short (~ a few tens of femtoseconds) to enable observations of the temporal evolution in a laser-irradiated nanowire array. To understand the absorption of laser energy in a laser-irradiated nanowire array, it is essential to perform time-resolved measurements on nanowire arrays with different spatial parameters. Recently, Sawada et al. proposed an ultrafast time-resolved measurement platform[44] that utilizes the SACLA x-ray free electron laser (XFEL) facility[45,46]. By using this platform, we conducted time-resolved measurements at SACLA facility on laser-irradiated nanowire arrays with several different spatial parameters.

In this paper, we report three issues: (1) establishing of nanowire array fabrication method by conventional template-assisted technique, (2) the transmittance calibration of x-ray shadowgraphs for nanowire array samples with the XFEL, and (3) initial experimental findings from laser irradiation experiments. This paper is structured as follows: Section 2 describes the details of our process for fabricating nanowire arrays. Section 3 discusses the fabrication conditions and their use in controlling the parameters of the nanowire array. Section 4 describes the experimental setup at SACLA that we used for studying the nanowire arrays and presents preliminary results from x-ray shadowgraph measurements. Finally, Section 5 summarizes our conclusions.

2. Nanowire array fabrication using an anodic aluminum oxide template

There are two main types of methods for fabricating nanowire arrays: the top-down and bottom-up approaches[47]. In top-down approaches (e.g., lithography), nanostructures are formed directly on the surface of a semiconductor using high-resolution lithography or ion beams. In contrast, bottom-up approaches involve the selective stacking of atoms or molecules on the surface of a material to form nanostructures. Although the former approach permits a high degree of pattern controllability, it is time-consuming, costly, and challenging to use for producing nanowires over large areas. In contrast, the bottom-up approach has the advantage of being cost effective, and it can be used to form nanostructures over large surface areas (~cm^2). However, the controllability of a structure produced using the bottom-up method is inferior to that produced by the top-down approach. As an alternative to both types of approaches, we have developed a method that employs an anodic aluminum oxide (AAO) template to produce nanowire arrays[48]. Figure 1 outlines this nanowire array fabrication process. In this template-based method, atoms are selectively stacked on the material surface, as in the bottom-up approach, but with more control over the structure. The AAO-template method consists of two steps: preparation of the AAO and then electroplating it. The AAO-template is a self-assembled nanostructure created by anodizing the aluminum. It contains many nanoholes that grow perpendicular to the bottom layer. The structure of the AAO-template is determined by the anodization conditions, and many fabrication conditions have been reported[49,50]. We explained the detailed AAO fabrication process in the Supplemental material. After creating the AAO-template, we plate it electrochemically to create a base layer and fill the nanoholes with metal. After the electroplating process, we dissolve the AAO using a NaOH solution, which leaves behind the nanowire array structure.

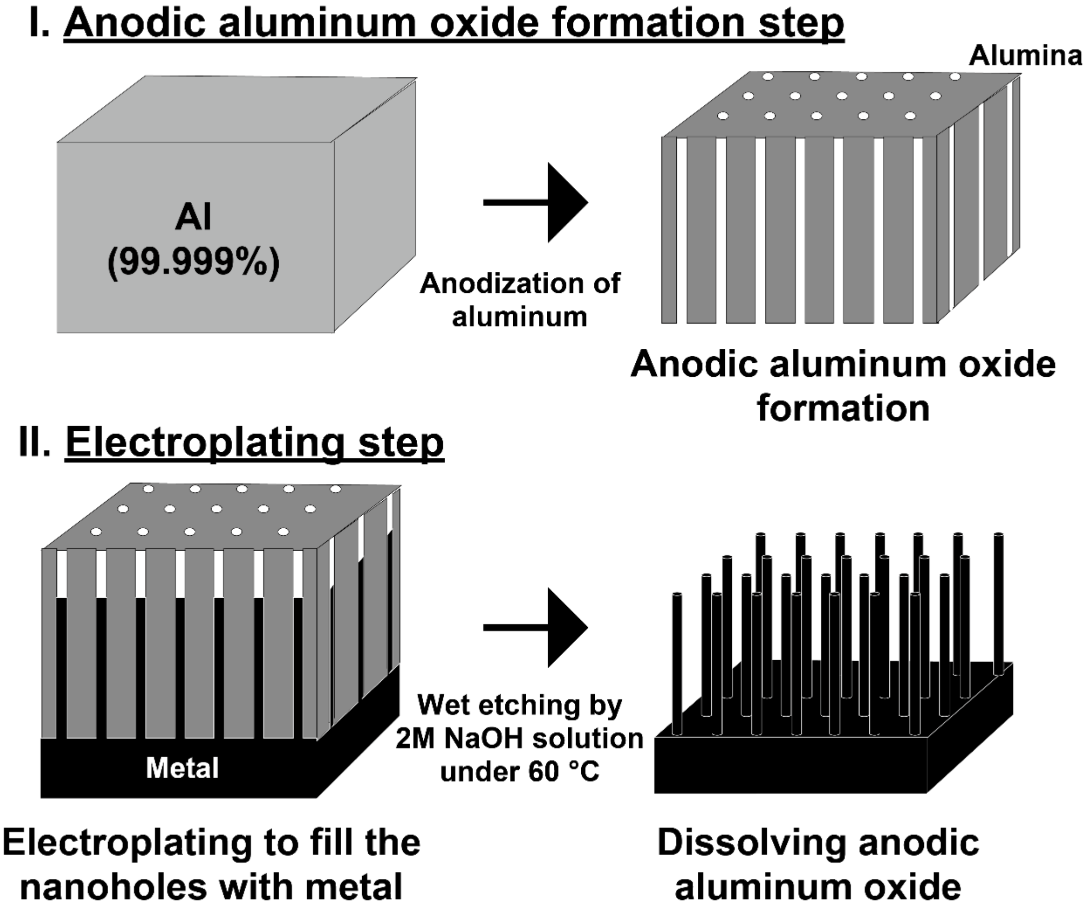

Figure 1 Illustration of the nanowire array fabrication steps.

2.1 Fabrication of a nanowire array by electrochemical deposition

We formed the nanowires and the base layer using an electroplating technique on the fabricated AAO. However, as AAO is a non-conducting material—and therefore cannot be electroplated—we sputtered 20 nm of Cr onto the bottom of the AAO as a wetting layer and then sputtered 100 nm of Au as a conducting layer. We performed the sputtering in 50-nm increments separated by 2-h cooling periods to minimize heating of the AAO membrane. Because the AAO is amorphous and crystallizes when heated[50], and because the crystallized

AAO becomes chemically insoluble, the process of etching with a NaOH solution, described below, would become impossible.

To create nanowire arrays, we employed electroplating to form the nanowires in the AAO after completing the sputtering process. We have optimized electrochemical deposition conditions for both Cu and Ni. Cu was deposited from a solution of 65 g/L CuSO4 •5H_2O, 1.4 g/L H_2SO_4, while Ni was deposited from a solution containing $NiSO_4$ •6H_2O, 300 g/L, 45 g/L $NiCl_2$ •6H_2O, and 45 g/L H_3BO_3. The wires and substrate were plated separately to control the wire length and substrate thickness. First, to plate only the base side, we painted the side on which Au had not been deposited with nail polish (mainly composed of ethyl acetate and cellulose acetate). After the base layer was formed, we removed the nail polish using acetone, and we then electroplated the nanohole side to fill the nanoholes with metal, thus forming the nanowires.

2.2 Processing of nanowire arrays as targets for laser-irradiation experiments

To use the nanowire arrays in experiments, they must be processed to form an appropriate target shape to be mounted in a sample holder. We used a femtosecond laser to cut the rear (base) side of the nanowire array, as shown in Fig. 2(a). This laser processing must be performed before dissolving the AAO with sodium hydroxide because the laser will otherwise melt the nanowires, and debris from the laser-cutting will adhere to the surface of the nanowire array, as shown in Fig. 2(b).

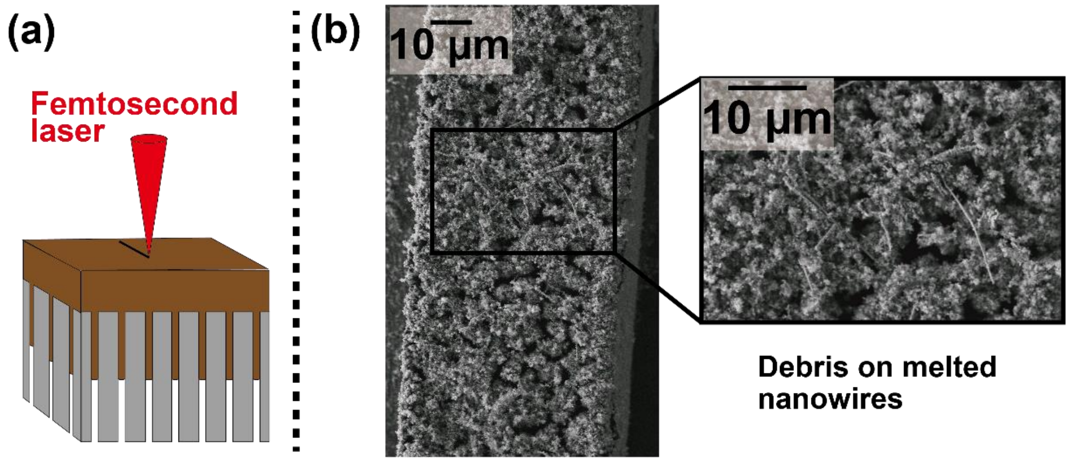

Figure 2 (a) Illustration of the laser-cutting process. (b) Scanning electron microscope (SEM) image of a nanowire array cut by a femtosecond laser after dissolving the AAO, recorded using a JEOL JSM-7400.

After the femtosecond laser processing, we immersed the nanowire arrays twice in a 2 M sodium hydroxide solution at 60 °C for 10 min to remove the AAO, after which we washed the nanowire arrays three times with Mili-Q water.

We then dried the nanowire arrays in a supercritical dryer. When nanowire arrays are dried in air, the nanowires aggregate due to surface tension. We therefore used a supercritical dryer to suppress the surface tension and prevent the nanowires from agglomerating[51]. Before processing them in the supercritical dryer, we immersed the washed nanowire arrays in acetone three times. We then placed the samples in the chamber of the supercritical dryer, which was filled with acetone. We took special care to prevent the nanowire arrays from drying in air in order to prevent the nanowires from agglomerating. We dried the samples in the supercritical dryer for at least 2 hours.

3. Controlling the spatial parameters of the nanowire arrays and materials by changing the fabrication conditions

3.1 Controlling the spatial parameters through the anodization and chemical-etching conditions.

As the spatial parameters of a nanowire array strongly affect its absorption of laser energy[39-41], those parameters must be controlled carefully. In our AAO-template nanowire array fabrication method, the diameters and arrangements of the nanowires are determined by the AAO fabrication conditions. The diameters and arrangements of the nanoholes are known to be determined by the voltages and reagents used in the anodization process[50]. Based on previous studies, we therefore tried various combinations of voltages and reagents to determine the optimal synthesis conditions. Table 1 summarizes the reagents, temperatures, voltages, and expected diameters for AAO fabrication. Figure 3(a) shows the relationship between the mean nanohole diameter and the anodic voltage; this figure shows that the hole diameter increases linearly with the anodization voltage, which is consistent with a previous study[50]. In addition, the mean diameter and filling factor of the nanowire array can be controlled simultaneously by adjusting the duration of immersion in phosphoric acid. Figure 3(b) shows the mean nanohole diameter *versus* the chemical-etching time in the phosphoric acid. Immersing the AAO in phosphoric acid for a long time dissolves the inner walls of the nanoholes in the AAO, which increases the mean hole diameter. Figures 3 (c)–(f) show examples of the fabricated AAO-template and the resulting nanowire arrays made of Cu. The nanowire diameter was controlled within the range 40–400 nm, and the filling factors were in the range of 13–40%.

Table 1 AAO fabrication conditions.

Solution	Voltage (V)	Temperature (°C)	Expected average diameter of nanoholes (nm)
Oxalic acid (0.3 M)	45–120	0 or 20	60–150
Phosphoric acid (0.1 M)	180	0	200

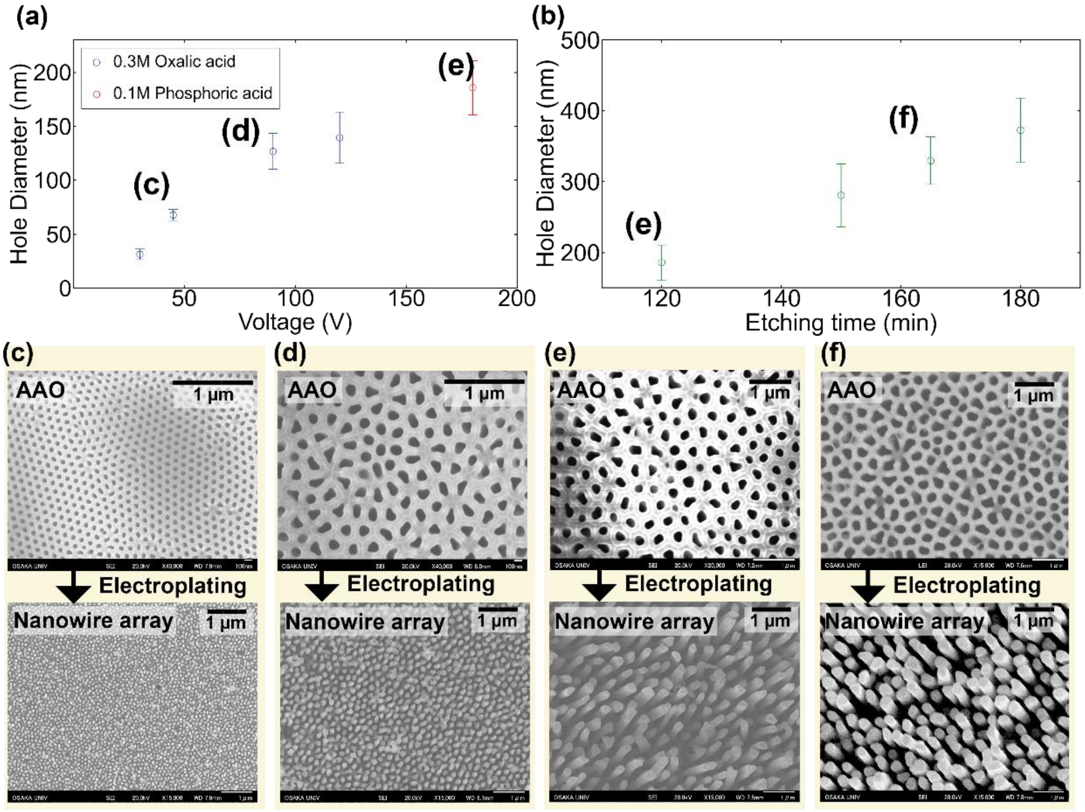

Figure 3 (a) The relationship between hole diameter and anodic voltage. The different colors indicate the solutions used for AAO fabrication: red is phosphoric acid, and blue is oxalic acid. (b) Plot of AAO etching rate in 20 wt% phosphoric acid. The error bars represent standard deviations. (c)–(f) SEM images of the AAO templates and the resulting nanowire arrays.

3.2 Controlling the electrochemical deposition process and evaluation of nanowire arrays

In the AAO-template method, the material of which the nanowire arrays are composed is determined by the electrochemical deposition process. The constituent material of a nanowire array is crucial for laser–plasma experiments because the characteristic x-rays emitted from the target are often used as diagnostics in such experiments[18]. Furthermore, the x-ray absorption spectrum is a critical item for ultrafast time-resolved measurements at SACLA. Figure 4 shows the photographs of Cu and Ni nanowire arrays. On the ultrahigh intensity laser experimental platform on the SACLA facility, the Cu-Kα emission imager based on a spherically bent crystal and other diagnostics for Cu is available, Cu is employed as standard target material compared in this experiment.

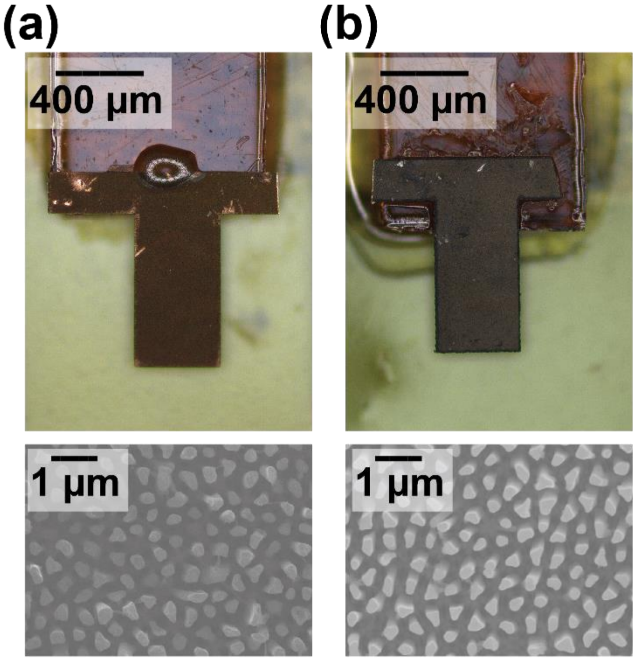

Figure 4 Optical microscope and SEM images of (a) Cu and (b) Ni nanowire arrays

To smooth the plated surface—especially for Cu—we added to the Cu-plating solution a so-called “brightener” that consisted of 400 ppm of polyethylene glycol, 60 ppm of HCl, and 30 ppm of Janus Green B. Figure 5 shows the difference in surface roughness with and without this brightener. Figure 5(a) shows the rear surface produced using a Cu-plating solution without the brightener; it exhibited many Cu grains 10–20 μm in size. In contrast, Figure 5(b) shows the rear surface obtained using a Cu-plating solution with the brightener; it also had many Cu grains, but with sizes now suppressed to 2–4 μm.

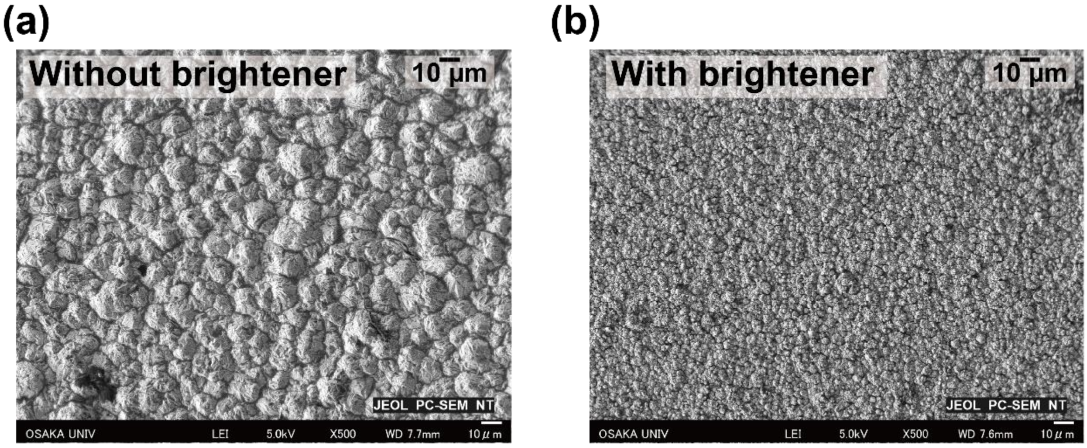

Figure 5 Comparison of Cu rear surfaces (a) without brightener and (b) with brightener.

We evaluated the crystallinity and impurity of the Cu nanowire with transmission electron microscopy (TEM), energy-dispersive x-ray spectroscopy (EDX), and selected area electron diffraction (SAED). Figure 6 (a) presents a high-angle annular dark field (HAADF) image for the Cu nanowire, with JEOL JEM-2100F, while Figures 6 (b)–(d) show corresponding elemental maps. We evaluated the impurities, specifically for oxygen, nitrogen, and chlorine, in the Cu nanowire. Oxygen would be from water immersion during etching and washing process, as well as storage in air prior to the experiment. Whereas the other two elements would be from the usage of brightener. Regarding oxygen, its signal was uniformly detected from the nanowire, indicating that the nanowire was oxidized. In the etching and washing process, Cu nanowires were immersed in water for approximately 10 minutes as we described in Section 2.2. This immersing time was significantly shorter than the ~6-hour oxidation period reported in previous work[52], so oxidation in water was not expected to be significant. On the other hand, the Cu nanowires were stored in air for less than two months before the experiment, potentially allowing some oxidation. Previous work indicated that less than ~10 nm of native oxide forms on high-purity copper films after about 1,000 hours of air exposure at room temperature[53]. Therefore, it was reasonable to expect a similar extent of oxidation here. As for the other two impurities (N and Cl), the signals for these elements were below the detection limit.

Figure 7 shows the blight field TEM image and SAED patterns of the nanowire. From the middle to the lower section of the nanowire (Figures 7(c) and (d)), clear single-crystal patterns were observed. In contrast, the SAED pattern of the upper part of the nanowire, as shown in Fig. 7(b), differed from the other two sections. A weak ring pattern corresponding to a polycrystalline phase was partially detected. According to the EDX data, gold, sputtered as a conductive layer on the bottom of the nanowire, was observed on the lower part of the nanowire. This indicates that the upper part of the nanowire corresponds to its tip. Fine particles attached to the tip influenced the SAED pattern. These measurements indicated that the majority of the fabricated nanowire consisted of single-crystal Cu.

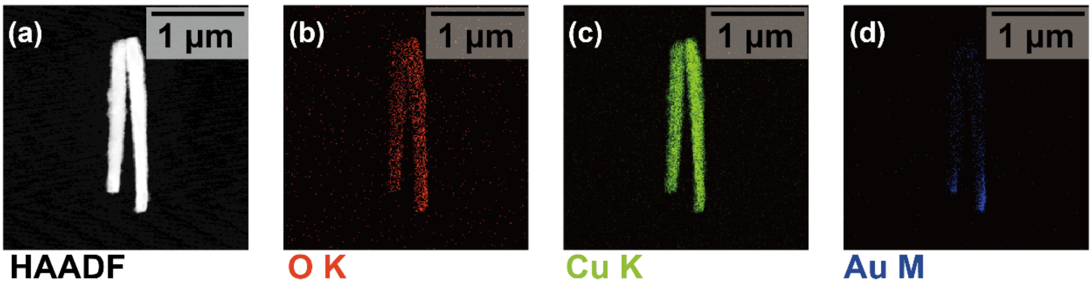

Figure 6 Energy dispersive x-ray spectroscopy (EDX) images. (a) HAADF image of the nanowires. Corresponding elemental mapping on the nanowire shown in (a). (b) Oxygen elemental mapping. (c)

Copper elemental mapping. (d) Gold elemental mapping

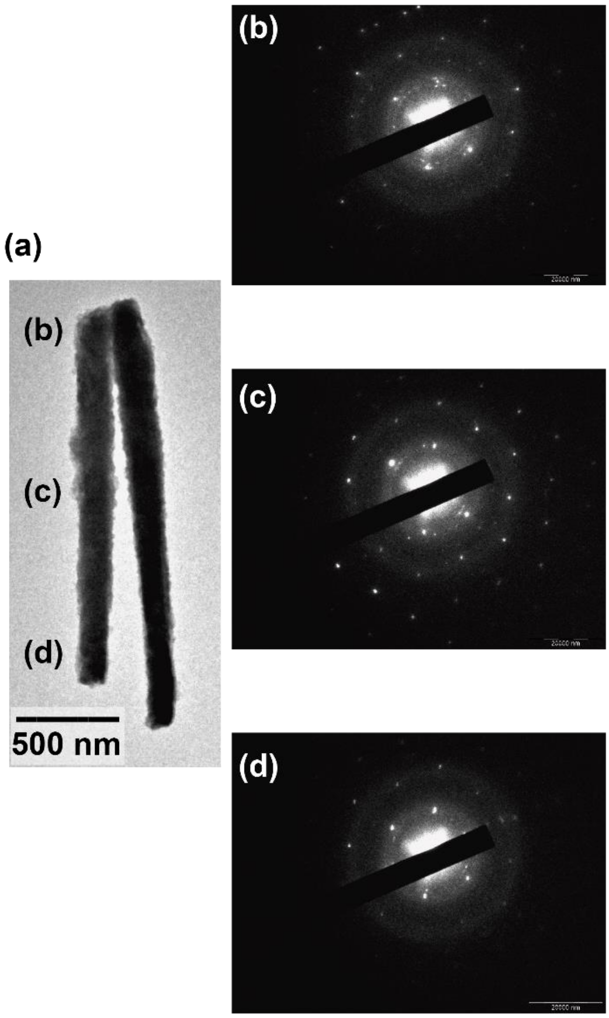

Figure 7 (a) Transmission electron microscope (TEM) images of the Cu nanowire. Selected area electron diffraction (SAED) pattern at (b) upper, (c) middle, and (d) lower part of the Cu nanowire.

4. Ultrafast time-resolved measurements performed at the SACLA facility

We performed experiments with several nanowire arrays in Experimental Hutch 6 (EH6) at SACLA Beamline 2 (BL2)[45,46]. Figure 8 shows the experimental setup. In these experiments, a collimated XFEL beam probed the target at an angle of incidence of 28° after the target had first been irradiated with a tightly focused beam from an ultrahigh intensity laser installed in EH6. We conducted the laser shots with changing the time delay (Δt) between the ultrahigh intensity laser and XFEL.

The XFEL photon energy was set to 8.92 keV or 8.05 keV, and its spectral bandwidth was ~30 eV at full width at half maximum (FWHM). Its pulse energy was approximately 300 µJ. We selected the XFEL photon energy to be less than the K-edge energy of Cu (~8.98 keV) in order to record the change in x-ray transmittance due to the change in temperature and density of the laser-irradiated target, which we describe later. The ultrahigh intensity laser irradiated the sample at an angle of incidence of 45° following reflection from an f/10 off-axis parabola; the pulse width was 30 fs (FWHM), the diameter of the focal spot was ~20 μm, the wavelength was 800 nm, and the laser energy delivered on target was 0.8~1.2 J. Table 2 and 3 summarizes the conditions of the ultrahigh intensity laser and XFEL, respectively.

Table 2 Summary of ultrahigh intensity laser conditions.

Intensity (W/cm^2)	**Laser energy (J)**	**Pulse width (fs)**	**Spot size (μm)**	**Incidence angle (°)**	**Wavelength (nm)**	**Pulse contrast**
$2 \sim 3 \times 10^{18}$	0.8~1.2 J	30 fs	~20	45	800	$\sim 10^{7}$ 10 ps before main pulse arrival

Table 3 Summary of XFEL conditions.

Pulse energy (μJ)	**Photon energy (keV)**	**Pulse width (fs)**	**Incidence angle (°)**	**Spectral bandwidth (eV)**
290	8.05	10 fs	28	30
320	8.92	10 fs	28	30

We took XFEL shadowgraphs with a 16-bit, scintillator-based CMOS camera having a pixel size of 6.5 μm and a total of 2048 × 2048 pixels (Hamamatsu Photonics ORCA-Flash4.0 V2)[54]. The camera used in the experiment series had magnifications of 10× and 20×, with spatial resolutions of 0.6 μm/pixel and 0.3 μm/pixel, respectively. The spatial resolution of the entire diagnostic system was 3 μm[44]. The pulse duration of the XFEL was around 10 fs, and the nominal jitter between the laser and the XFEL was ~100 fs[46]; the temporal resolution of the x-ray shadowgraph can be evaluated from these two values. We also monitored the laser–plasma interaction with an x-ray spectrometer, a Cu-Kα imager, and an electron spectrometer.

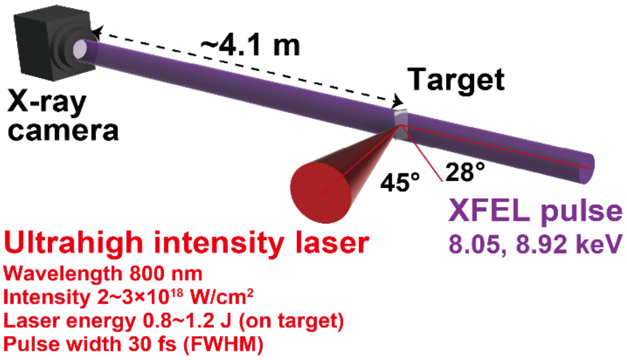

Figure 8 Schematic of the experimental setup.

We employed four kinds of targets in the experiments. By changing the nanowire array fabrication conditions as described in Sections 2 and 3, we fabricated three kinds of nanowire arrays: standard, dense, and long. The standard nanowire array had a low filling factor and short wire lengths. The diameter of each nanowire array was set to as approximately 200 nm. To reduce the pre-pulse effect in our experiments, we employed nanowire arrays with a diameter of 200 nm and the largest achievable gap (~480 nm). As explained in Section 1, ultrahigh intensity lasers have a pre-pulse, a weak-intensity laser pulse that precedes the main pulse. This pre-pulse can ionize target materials, forming a thin plasma layer before the main pulse arrives. In nanowire arrays, the pre-pulse can fill the gaps between the wires with plasma, inhibiting the penetration of the main pulse into the interior of the nanowire array. To mitigate this plasma-filling effect, we selected a nanowire array with the widest achievable gap (~480 nm) in our fabrication technique. Each nanowire array is characterized here by the following parameters: the wire diameter d (nm), the gap g (nm), the length L (µm), the number density of wires $D = 1/g^2$ (1/µm^2), and the filling factor $FF = \pi \times (d/2)^2 \times D$. L for each nanowire array target was evaluated by the cross-sectional view by the SEM observation. As reference targets, we also employed flat Cu foils, each 10 µm thick. The nanowire arrays and foils were cut into the 900×400 µm^2 pieces by femtosecond laser as described in Section 2.2. All targets were stored in the clean room for less than two months before the experiment. Therefore, although a thin oxide layer (less than 10 nm[53]) could have formed on the target surface, it is expected to have minimal impact on the target initial density. The detailed specifications of each nanowire array are summarized in Table 4, and SEM images of each target are displayed in Fig. 9.

Table 4 Summary of target conditions.

Target type	**Filling factor (dimensionless)**	**Diameter d (nm)**	**Gap g (nm)**	**Number density D (1/µm^2)**	**Length L (µm)**
Standard nanowire array	0.13	~200	480	4.3	2.5

Long nanowire array	0.13	~200	480	4.3	13
Dense nanowire array	0.40	~200	280	12.8	2.5
Cu flat foil	-	-	-	-	10

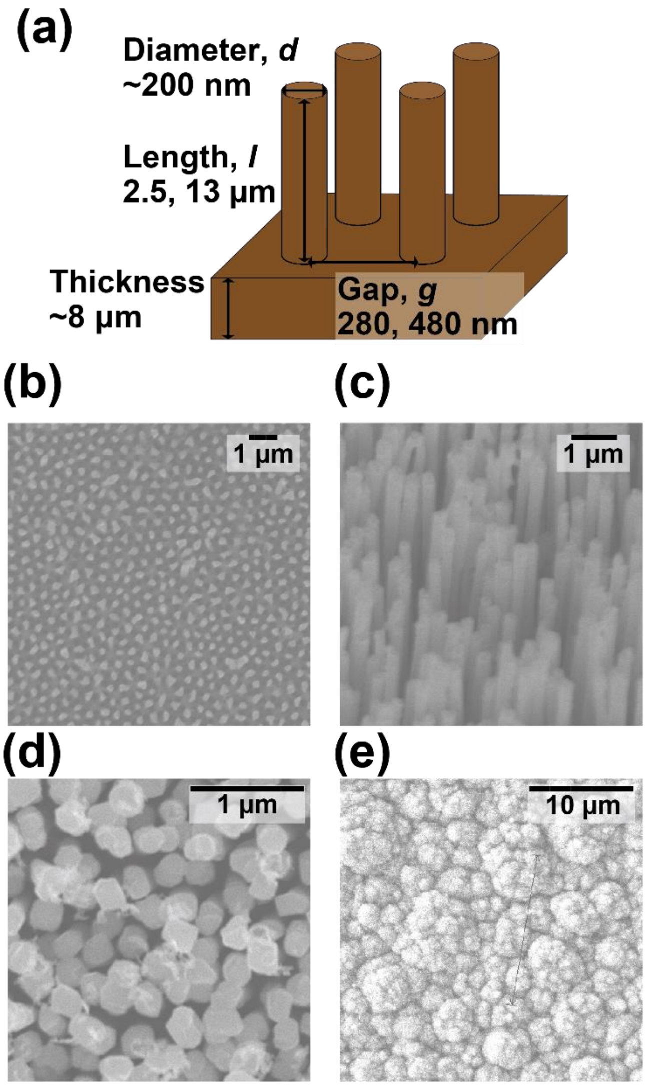

Figure 9 The nanowire targets used in the experiments: (a) Schematic illustration of a nanowire array. Scanning electron microscope (SEM) images of the (b) standard, (c) long, and (d) dense nanowire arrays. (e) SEM image of the rear side of a nanowire array.

4.1 Static x-ray shadowgraphs of nanowire array targets

Figures 10(a) and 10(b) present x-ray shadowgraph images of the Cu flat foil and the long nanowire array, respectively, obtained with the XFEL beam incident at an angle of 28°. Figure 10(c) shows post-processed one-dimensional line profiles of each target.

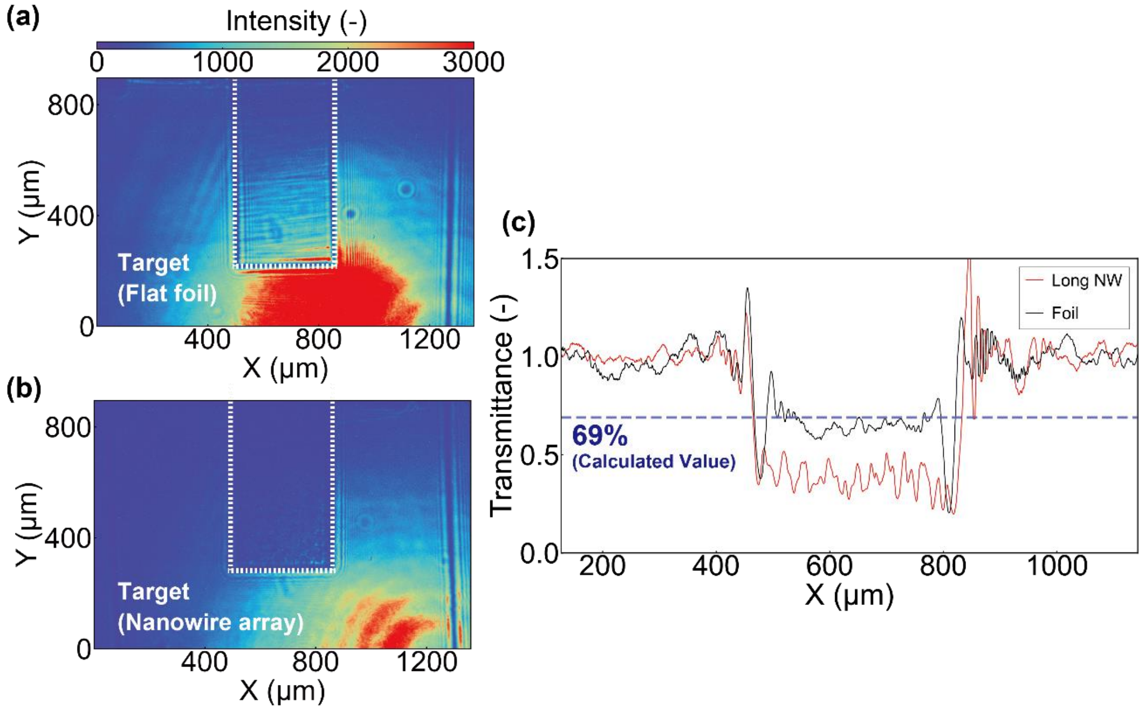

Figure 10 X-ray shadowgraph images of (a) a flat Cu foil and (b) the long nanowire array. (c) One-dimensional line profiles of the flat foil and the long nanowire array. The line profile shown was smoothed using a median filter with a size equivalent to the spatial resolution. The dotted blue line shows the transmittance value calculated from the database at the Center for X-ray Optics (CXRO)[55].

Although the areal densities of the Cu flat foil and the long nanowire array had almost the same value, we observed a weaker x-ray signal intensity in the shadowgraph of the long nanowire array. We evaluated the x-ray transmittance of the three different nanowire array targets by comparing the reductions in the intensity of x-rays transmitted through them[44]. First, we obtained a one-dimensional (1D) line profile of the x-ray intensity, *I(x)*, across the whole shadowgraph by integrating and averaging the shadowgraph signals longitudinal to 10 pixels in the vertical direction, corresponding to the spatial resolution. We then used a double-gaussian approximation to construct a reference profile $I_0(x)$ from the 1D-profile signals in regions where no target was present[44]. By dividing $I(x)$ by $I_0(x)$, we obtained a 1D transmittance profile [$T(x) = I(x)/I_0(x)$] for each target. The same procedure was applied for the vertical direction of the target, and the average value was taken as the target transparency. The error for each target was defined as the standard deviation of the measured lineouts. For the flat foil, the resulting x-ray transmittance matched well with the value calculated from the database at the Center for X-ray Optics (CXRO) [55]. (Note that the thickness of the Cu flat foil had a 10% uncertainty according to the vendor.) In contrast, we observed a 42% decrease in x-ray transmittance for the long nanowire array. We performed the same type of analysis for the standard and dense nanowire arrays, and the results are summarized in Table 5.

Table 5 Summary of transmittance (*T*) values for different targets.

Target	***T* (Calculated)**	***T* (Experimental)**	**Ratio {*T*(Experimental)/*T*(Calculated)}**
10 μm Cu flat foil	0.69	0.66±0.01	0.96±0.01
Long nanowire array	0.69	0.40±0.02	0.58±0.03
Dense nanowire array	0.71	0.53±0.02	0.75±0.03
Standard nanowire array	0.73	0.64±0.03	0.87±0.04

As Table 5 shows, a reduction in the transmitted x-ray intensity was confirmed for every nanowire array. As described in Section 3.2, the nanowire array presented in this study exhibited small Cu grains, approximately a few micrometers in size, on its rear surface. Although the size of the Cu grains was small, the effect on the x-ray shadowgraph analysis is not negligibly small[44]. This is one of the reason why the transmittance value of the nanowire array had a larger error compared to that of the flat foil with smoother surface. The reduction effect of the nanowire array is thought to be caused by x-ray scattering by the nanowires. Unlike the Cu flat foil, in the nanowire arrays there are numerous nanowires perpendicular to the surface of the substrate. Some x-rays are therefore incident on the wires at very small angles, causing attenuation of the x-ray intensity incident on the scintillator.

To understand this effect, we introduced the normalized surface area: *NSA,* defined as $NSA \equiv \left\{\pi\left(\frac{d}{2}\right)^2 + \pi d h\right\} \times D$, where h is the x-ray penetration depth, and we used the value of wire length for each nanowire array was used as an h value. Figure 11 shows the ratio the experimental to the calculated x-ray absorption *versus* the *NSA* value for each target. By using the *NSA*, we can take into account not only the cross-sectional area but also the lateral surface areas of the nanowires; this enables us to include the effect of the nanowires interacting with the x-rays more accurately than by using the filling factor.

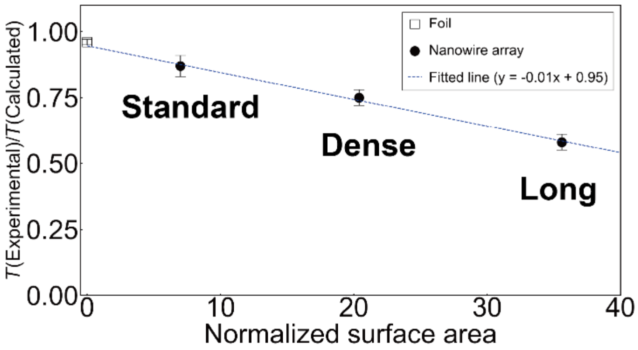

Figure 11 Ratio of measured and calculated transmitted x-ray light intensity *versus* the (dimensionless) normalized surface area.

Figure 11 shows that as the *NSA* value increases, the transmittance ratio decreases. By fitting a first-order linear relation to the dataset from the nanowire array targets, we can also estimate the attenuation of the x-ray signal due to the roughness of the rear surface caused by the plating described in Section 3. When *NSA* = 0 (i.e., when there are no nanowires), the ratio was approximately 5%; this reduction in the transmitted x-ray intensity is due to the roughness of the rear surface, which adds to the reduction due to the nanowires.

4.2 Preliminary experimental results: time-resolved x-ray-shadowgraph imaging with ultrahigh intensity laser-irradiation

We obtained time-resolved, two-dimensional x-ray shadowgraphs of the laser-irradiated targets by varying the time delay.

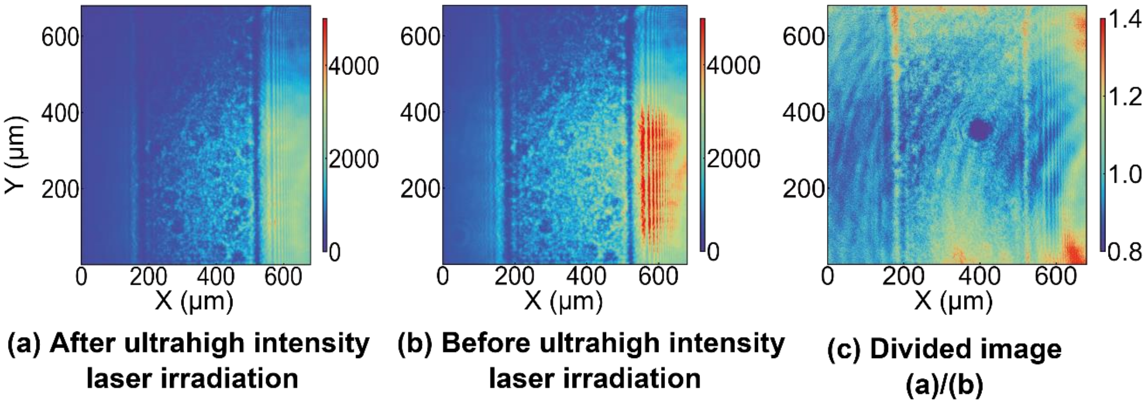

(a) After ultrahigh intensity laser irradiation

(b) Before ultrahigh intensity laser irradiation

(c) Divided image (a)/(b)

Figure 12 Shadowgraph images taken (a) after and (b) before ultrahigh intensity laser-irradiation. (c) Divided image: ratio of (b) to (a).

Figures 12(a) and 12(b) show x-ray shadowgraph images of the standard nanowire array before and after ultrahigh intensity laser-irradiation. A slight decrease in x-ray transmittance due to the K-edge shift effect[44,56-58] is observed in Fig. 12(b), but evaluating the size of the heated area in the raw image is not straightforward. In addition, it was much harder to evaluate the areas for which the transmittance was affected because the nanowire array reduced the transmitted x-ray intensity. To observe the changes in x-ray transmittance with better contrast, we therefore divided these two images, and the divided image shown in Fig. 12(c)[44,58]. This figure shows the changes in x-ray transmittance clearly; in particular, the region heated by the drive laser and hot electrons is the darkened spot in the center of this image. Figure 13 shows the divided image and the transmittance ratio for each target. By dividing the two images, we have thus successfully evaluated the transmittance change that occurred in each target and minimized the reduction in the x-ray intensity transmitted through the nanowire array.

Figures 13 (a)–(c) show divided images for flat foil, standard, and dense nanowire arrays from the x-ray shadowgraph measurements. Please note that Δt value shown here had the ±0.1 ps error value due to the timing jitter between ultrahigh intensity laser and XFEL as we described in the beginning of Section 4. Compared to these images, the area where transmittance changed was significantly larger for the flat foil than for either the standard or dense nanowire arrays. This suggests that the size of the heated area with the laser irradiation and hot electrons was deduced for standard and dense nanowire arrays. As discussed in our previous work[41], the nanowire array can reduce energy scattering by suppressing surface currents and forming periodic intense magnetic fields. The smaller transmittance change region in the nanowire arrays implies that energy dissipation was minimized, and heating by hot electrons was dominant in a narrower region compared to the flat foil.

Figure 13(d) shows the transmittance changes in the long nanowire array. Unlike other targets, the transmittance changes in the long nanowire array were the most ambiguous among all the targets. A possible explanation for this is that the K-edge shift was more significant for the long nanowire array due to a greater increase in electron temperature than in other targets. As a result, the x-ray transmittance returned to its ambient-state value, making the observed changes in x-ray transmittance less distinct.

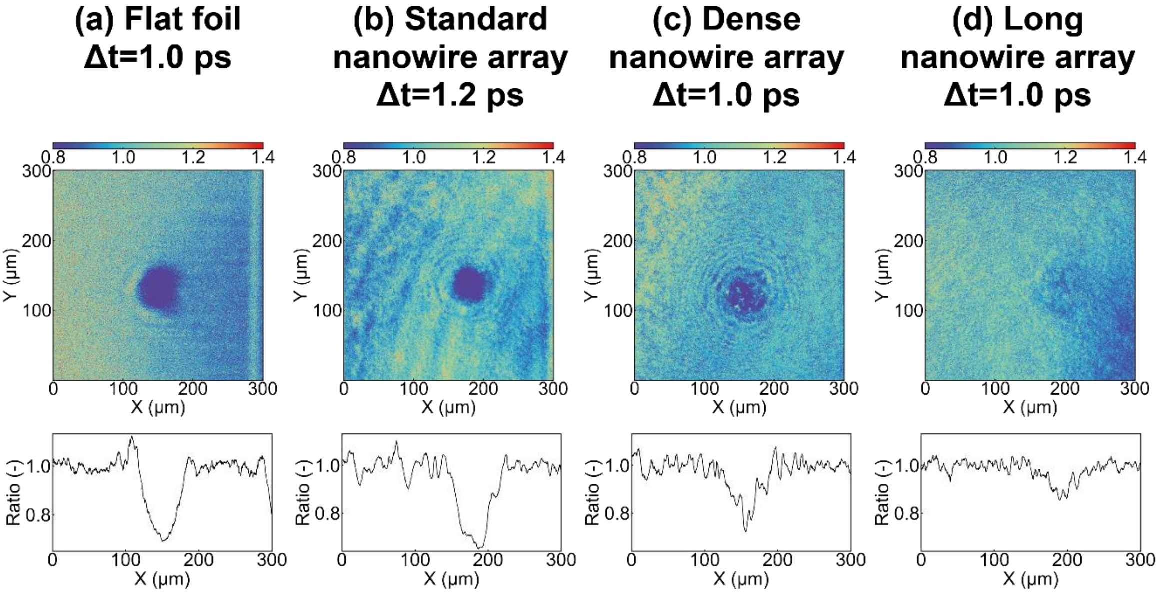

Figure 13 Divided images and line profiles for (a) flat foil, (b) standard, (c) dense, and (d) long nanowire arrays.

We also evaluated changes in "shape" of nanowires using x-ray shadowgraph observations. As discussed in Section 4.1, transmitted x-ray intensity is reduced for nanowire array due to x-ray scattering. When the shape of the nanowires deformed and smoothed out after laser irradiation, the reduction on the transmitted x-ray intensity is expected to be small. In order to verify the effect, we measured the increase in x-ray transmittance caused by the shape changes in the nanowires using x-ray shadowgraphs at a photon energy of 8.05 keV, far away from the K-edge of Cu. Figure 14 shows x-ray shadowgraph images of the dense nanowire array after laser irradiation. Up to 5 ps after laser irradiation, no significant increase in x-ray transmittance was observed as shown in Fig.14 (a). According to Fig. 14 (b) and (c), x-ray transmittance started to be increased at *Δt* of 10 ps. This indicates that the nanowire array maintained its shape up to 5 ps after the laser irradiation. Therefore, the effect of shape changes in the nanowires is negligible throughout the observation timing in this study (up to a few picoseconds).

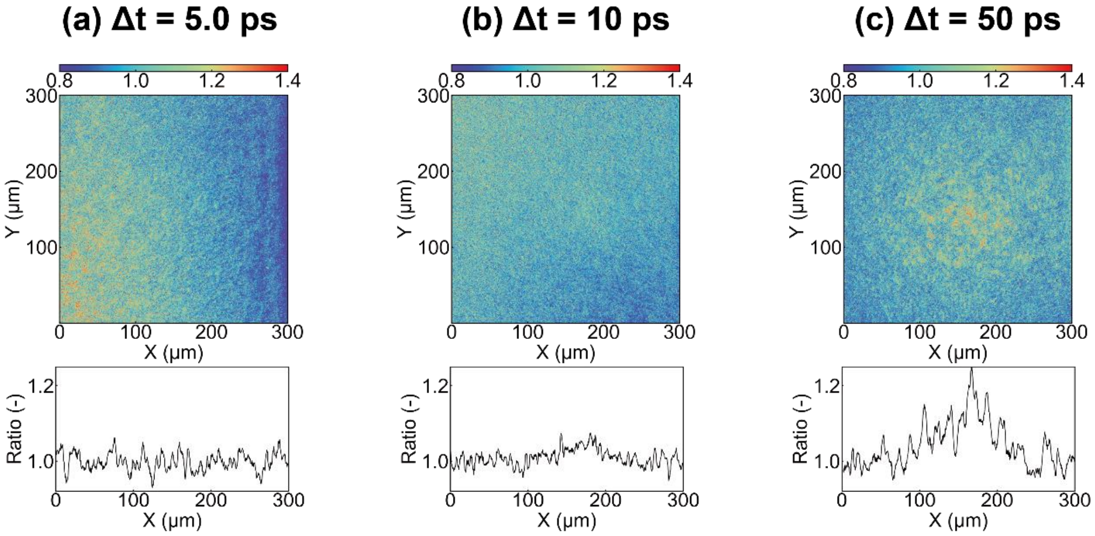

Figure 14 X-ray shadowgraph images and corresponding line profiles of a dense nanowire array recorded at Δt = (a) 5.0 ps, (b) 10 ps, and (c) 50 ps.

5. Conclusion

We present the first experimental results on ultrafast dynamics measurement with high-spatial and time resolution for nanowire array irradiated with ultrahigh intensity laser at SACLA X-ray free-electron-laser facility. First, to establish the fabrication method of nanowire arrays for the experiments, we employed an AAO-template method. By exploring various AAO fabrication and electroplating conditions, we have successfully fabricated nanowire array targets made of Cu or Ni, with nanowire diameters ranging from 60 nm to 400 nm, filling factors from 13% to 40%, and nanowire lengths up to 13 μm. We also characterized the fabricated nanowire using EDX and SAED in TEM. EDX analysis revealed that the thin surface of the fabricated nanowire was oxidized. SAED observation indicated that the majority of the fabricated nanowires consisted of a single-crystal Cu.

On the laser irradiation experiments, we performed the calibration of x-ray transmittance for nanowire arrays. We observed that the nanowire arrays reduced the transmitted x-ray intensities. We also observed that this reduction effect became stronger as the surface area of the nanowire array that interacted with the x-ray irradiation was increased. The transmitted x-ray intensity was also reduced by the surface roughness on the rear side of the target; this had a significant effect on the x-ray shadowgraph. However, the surface roughness was improved by the addition of a brightener.

We successfully recorded ultrafast, time-resolved x-ray shadowgraphs at EH6 of SACLA using nanowire arrays fabricated with different spatial parameters. In the obtained data, we observed changes in the x-ray transmittance due to laser and hot-electron heating and confirmed that the nanowire array structure was kept in a few picoseconds after the irradiation.

Further analysis of these results is still required, and we plan to clarify the detailed mechanisms by comparing the results with PIC simulation calculations. We will report the details of these experimental results in an upcoming paper.

Supplemental material

See the supplementary material for the detailed process of the AAO fabrication.

Acknowledgments

The XFEL experiments were performed at the BL2 of SACLA with the approval of the Japan Synchrotron Radiation Research Institute (JASRI) (Proposal No. ,2023A8015, 2023A8018, 2021B8070). This work was performed under the Institute of Laser Engineering (ILE) joint research project, Osaka University (under contract subject 2023B2-018SAWADA). The authors would like to acknowledge the dedicated technical support provided by the staff at the SACLA for the XFEL operation and x-ray diagnostics. D. T. was supported by the Japan Society for the Promotion of Science, (KAKENHI Grant No. 23KJ1526). D. T. also would like to acknowledge the SACLA Research Support Program for Graduate Students. H. S. was supported by the National Science Foundation under Grant No. 2010502 through the NSF/DOE Partnership in Basic Plasma Science and Engineering.

Author contributions

D. Tanaka: Data Curation (equal); Formal analysis (lead); Investigation (equal); Visualization (lead); Resources (lead); Funding acquisition (support); Writing – original draft (lead); Writing – review & editing (lead).
H.Sawada: Data Curation (equal); Formal analysis (support); Investigation (equal); Funding acquisition (support); Methodology (supporting); Writing – review & editing (equal).
T.Idesaka: Data Curation (equal); Investigation (equal).
C.Nakatsuji: Data Curation (equal); Investigation (equal).
S.Matsuura: Data Curation (equal); Investigation (equal).
T.Sato: Data Curation (equal); Investigation (equal).
T.Somekawa: Resources (equal).
T.Yabuuchi: Investigation (equal); Resources (equal); Writing – review & editing (equal).
K.Miyanishi: Investigation (equal); Resources (equal).
K.Sueda: Investigation (equal); Resources (equal)
Y.Inubushi: Investigation (equal); Resources (equal).
Y.Sentoku: Writing – review & editing (equal).
T.Shimizu: Resources (equal) ; Writing – review & editing (equal).
S.Shingubara: Resources (equal).
K.Kawasaki: Writing – review & editing (equal).
N.Ozaki: Writing – review & editing (equal).
K.Yamanoi: Writing – review & editing (equal).
K.Shigemori: Conceptualization(lead); Data Curation (equal); Investigation (equal); Funding acquisition (lead); Project administration (lead); Methodology (lead); Supervision (lead);

Writing – review & editing (equal).

Conflict of interest

The authors have no conflicts to declare.

Data availability

The data that support the findings of this study are available from the corresponding author upon reasonable request.

Reference

1 D. Strickland and G. Mourou, “Compression of amplified chirped optical pulses”, Opt. Commun. 56(3), 219–221 (1985). [DOI]: 10.1016/0030-4018(85)90120-8

2 M. Tabak, J. Hammer, M. E. Glinsky, W. L. Kruer, S. C. Wilks, J. Woodworth, E. M. Campbell, M. D. Perry, and R. J. Mason, “Ignition and high gain with ultrapowerful lasers”, Phys. Plasmas 1(5), 1626-1634 (1994) [DOI]: 10.1063/1.870664

3 R. Kodama, P. A. Norreys, K. Mima, A. E. Dangor, R. G. Evans, H. Fujita, Y. Kitagawa, K. Krushelnick, T. Miyakoshi, N. Miyanaga, T. Norimatsu, S. J. Rose, T. Shozaki, K. Shigemori, A. Sunahara, M. Tampo, K. A. Tanaka, Y. Toyama, T. Yamanaka, and M. Zepf, “Fast heating of ultrahigh-density plasma as a step towards laser fusion ignition”, Nature 412(6849), 798-802 (2001) [DOI]: 10.1038/35090525.

4 K. Matsuo, N. Higashi, N. Iwata, S. Sakata, S. Lee, T. Johzaki, H. Sawada, Y. Iwasa, K. F. F. Law, H. Morita, Y. Ochiai, S. Kojima, Y. Abe, M. Hata, T. Sano, H. Nagatomo, A. Sunahara, A. Morace, A. Yogo, M. Nakai, H. Sakagami, T. Ozaki, K. Yamanoi, T. Norimatsu, Y. Nakata, S. Tokita, J. Kawanaka, H. Shiraga, K. Mima, H. Azechi, R. Kodama, Y. Arikawa, Y. Sentoku, and S. Fujioka, “Petapascal pressure driven by fast isochoric heating with a multipicosecond intense laser pulse”, Phys. Rev. Lett. 124(3), 035001 (2020) [DOI]: 10.1103/PhysRevLett.124.035001.

5 X. Wang, R. Zgadzaj, N. Fazel, Z. Li, S.A. Yi, X. Zhang, W. Henderson, Y.Y. Chang, R. Korzekwa, H.E. Tsai, C.H. Pai, H. Quevedo, G. Dyer, E. Gaul, M. Martinez, A.C. Bernstein, T. Borger, M. Spinks, M. Donovan, V. Khudik, G. Shvets, T. Ditmire, and M.C. Downer, “Quasi-monoenergetic laser-plasma acceleration of electrons to 2 GeV,” Nat Commun 4, (2013) [DOI]:10.1038/ncomms2988.

6 M.C. Downer, R. Zgadzaj, A. Debus, U. Schramm, and M.C. Kaluza, “Diagnostics for plasma-based electron accelerators,” Rev Mod Phys 90(3), (2018) [DOI]: 10.1103/RevModPhys.90.035002.

7 C. Aniculaesei, T. Ha, S. Yoffe, L. Labun, S. Milton, E. McCary, M.M. Spinks, H.J. Quevedo, O.Z. Labun, R. Sain, A. Hannasch, R. Zgadzaj, I. Pagano, J.A. Franco-Altamirano, M.L. Ringuette, E. Gaul, S. V. Luedtke, G. Tiwari, B. Ersfeld, E. Brunetti, H. Ruhl, T. Ditmire, S. Bruce, M.E. Donovan, M.C. Downer, D.A. Jaroszynski, and B.M. Hegelich, “The acceleration of a high-charge electron bunch to 10

GeV in a 10-cm nanoparticle-assisted wakefield accelerator," Matter Radiat. Extremes 9(1), (2024) [DOI]: 10.1063/5.0161687.

8 R. Zgadzaj, J. Welch, Y. Cao, L.D. Amorim, A. Cheng, A. Gaikwad, P. Iapozzutto, P. Kumar, V.N. Litvinenko, I. Petrushina, R. Samulyak, N. Vafaei-Najafabadi, C. Joshi, C. Zhang, M. Babzien, M. Fedurin, R. Kupfer, K. Kusche, M.A. Palmer, I. V. Pogorelsky, M.N. Polyanskiy, C. Swinson, and M.C. Downer, "Plasma electron acceleration driven by a long-wave-infrared laser," Nat Commun 15(1), (2024) [DOI]: 10.1038/s41467-024-48413-y.

9 A. Picksley, J. Stackhouse, C. Benedetti, K. Nakamura, H.E. Tsai, R. Li, B. Miao, J.E. Shrock, E. Rockafellow, H.M. Milchberg, C.B. Schroeder, J. van Tilborg, E. Esarey, C.G.R. Geddes, and A.J. Gonsalves, "Matched Guiding and Controlled Injection in Dark-Current-Free, 10-GeV-Class, Channel-Guided Laser-Plasma Accelerators," Phys Rev Lett 133(25), 255001 (2024) [DOI]: 10.1103/PhysRevLett.133.255001.

10 T.M. Ostermayr, C. Kreuzer, F.S. Englbrecht, J. Gebhard, J. Hartmann, A. Huebl, D. Haffa, P. Hilz, K. Parodi, J. Wenz, M.E. Donovan, G. Dyer, E. Gaul, J. Gordon, M. Martinez, E. Mccary, M. Spinks, G. Tiwari, B.M. Hegelich, and J. Schreiber, "Laser-driven x-ray and proton micro-source and application to simultaneous single-shot bi-modal radiographic imaging," Nat Commun 11(1), (2020) [DOI]: 10.1038/s41467-020-19838-y.

11 F.H. Lindner, E. McCary, X. Jiao, T.M. Ostermayr, R. Roycroft, G. Tiwari, B.M. Hegelich, J. Schreiber, and P.G. Thirolf, "En-route to the fission-fusion reaction mechanism: A status update on laser-driven heavy ion acceleration," Plasma Phys Control Fusion 61(5), (2019) [DOI]: 10.1088/1361-6587/ab068d .

12 H. Daido, M. Nishiuchi, and A. S. Pirozhkov, "Review of laser-driven ion sources and their applications", Rep. Prog. Phys. 75(5), 056401 (2012) [DOI]: 10.1088/0034-4885/75/5/056401.

13 X. Jiao, C.B. Curry, M. Gauthier, H.G.J. Chou, F. Fiuza, J.B. Kim, D.D. Phan, E. McCary, E.C. Galtier, G.M. Dyer, B.K. Ofori-Okai, L. Labun, O.Z. Labun, C. Schoenwaelder, R. Roycroft, G. Tiwari, G.D. Glenn, F. Treffert, S.H. Glenzer, and B.M. Hegelich, "High deuteron and neutron yields from the interaction of a petawatt laser with a cryogenic deuterium jet" Front Phys 10, (2023) [DOI]: 10.3389/fphy.2022.964696.

14 G. Pretzler, A. Saemann, A. Pukhov, D. Rudolph, T. Schä, U. Schramm, P. Thirolf, D. Habs, K. Eidmann, G.D. Tsakiris, J. Meyer-Ter-Vehn, and K.J. Witte, "Neutron production by 200 mJ ultrashort laser pulses" Phys. Rev. E 58, 1165-1168 (1998) [DOI]: 10.1103/PhysRevE.58.1165.

15 Z. Lan, Y. Arikawa, S.R. Mirfayzi, A. Morace, T. Hayakawa, H. Sato, T. Kamiyama, T. Wei, Y. Tatsumi, M. Koizumi, Y. Abe, S. Fujioka, K. Mima, R. Kodama, and A. Yogo, "Single-shot laser-driven neutron resonance spectroscopy for temperature profiling," Nat Commun 15(1), (2024) [DOI]: 10.1038/s41467-024-49142-y .

16 F. Albert, "Principles and applications of x-ray light sources driven by laser wakefield acceleration," Phys Plasmas 30(5), (2023) [DOI]: 10.1063/5.0142033.

17 P.M. King, D. Rusby, A. Hannasch, N. Lemos, G. Tiwari, A. Pak, S. Kerr, G. Cochran, I. Pagano, G.J. Williams, S.F. Khan, M. Aufderheide, A. Kemp, S. Wilks, A. Macphee, F. Albert, B.M. Hegelich, M. Downer, M. Manuel, Z. Gavin, A. Haid, and A. Mackinnon, "Enhancement of high energy X-ray radiography using compound parabolic concentrator targets," High Energy Density Phys 42, (2022) [DOI]: 10.1016/j.hedp.2022.100978.

18 H. Sawada, S. Lee, T. Shiroto, H. Nagatomo, Y. Arikawa, H. Nishimura, T. Ueda, K. Shigemori, A. Sunahara, N. Ohnishi, F. N. Beg, W. Theobald, F. Pérez, P. K. Patel, S. Fujioka, "Flash Kα radiography of laser-driven solid sphere compression for fast ignition" Appl. Phys. Lett. 108 (25) (2016) [DOI]: 10.1063/1.4954383

19 E. Gaul, T. Toncian, M. Martinez, J. Gordon, M. Spinks, G. Dyer, N. Truong, C. Wagner, G. Tiwari, M.E. Donovan, T. Ditmire, and B.M. Hegelich, "Improved pulse contrast on the Texas Petawatt Laser," in J Phys Conf Ser, (2016) [DOI]: 10.1088/1742-6596/717/1/012092.

20 H. Kiriyama, A.S. Pirozhkov, M. Nishiuchi, Y. Fukuda, K. Ogura, A. Sagisaka, Y. Miyasaka, H. Sakaki, N.P. Dover, K. Kondo, H.F. Lowe, A. Kon, J.K. Koga, T.Z. Esirkepov, N. Nakanii, K. Huang, M. Kando, and K. Kondo, "Status and progress of the J-KAREN-P high intensity laser system at QST," High Energy Density Phys 36, (2020) [DOI]: 10.1016/j.hedp.2020.100771.

21 Y. Arikawa, S. Kojima, A. Morace, S. Sakata, T. Gawa, Y. Taguchi, Y. Abe, Z. Zhang, X. Vaisseau, S.H. Lee, K. Matsuo, S. Tosaki, M. Hata, K. Kawabata, Y. Kawakami, M. Ishida, K. Tsuji, S. Matsuo, N. Morio, T. Kawasaki, S. Tokita, Y. Nakata, T. Jitsuno, N. Miyanaga, J. Kawanaka, H. Nagatomo, A. Yogo, M. Nakai, H. Nishimura, H. Shiraga, S. Fujioka, FIREX Group, LFEX Group, H. Azechi, A. Sunahara, T. Johzaki, T. Ozaki, H. Sakagami, A. Sagisaka, K. Ogura, A.S. Pirozhkov, M. Nishikino, K. Kondo, S. Inoue, K. Teramoto, M. Hashida, and S. Sakabe, "Ultrahigh-contrast kilojoule-class petawatt LFEX laser using a plasma mirror" Appl Opt **55**(25), 6850 (2016) [DOI]: 10.1364/AO.55.006850 .

22 L. Fedeli, A. Sgattoni, G. Cantono, D. Garzella, F. Réau, I. Prencipe, M. Passoni, M. Raynaud, M. Květoň, J. Proska, A. Macchi, and T. Ceccotti, "Electron acceleration by relativistic surface plasmons in laser-grating interaction", Phys. Rev. Lett. 116(1), 015001 (2016) [DOI]: 10.1103/PhysRevLett.116.015001

23 W.-M. Wang, Z.-M. Sheng, and J. Zhang, "A model for the efficient coupling between intense lasers and subwavelength grating targets", Phys. Plasmas 15(3) (2008) [DOI]: 10.1063/1.2898456.

24 G. Cristoforetti, F. Baffigi, F. Brandi, G. D'Arrigo, A. Fazzi, L. Fulgentini, D. Giove, P. Koester, L. Labate, G. Maero, D. Palla, M. Romé, R. Russo, D. Terzani, P. Tomassini, and L. A. Gizzi, "Laser-driven proton acceleration via excitation of surface plasmon polaritons into TiO2nanotube array targets", Plasma Phys. Control. Fusion 62(11) (2020) [DOI]: 10.1088/1361-6587/abb5e3

25 H. A. Sumeruk, S. Kneip, D. R. Symes, I. V. Churina, A. V. Belolipetski, T. D. Donnelly, and T. Ditmire, "Control of strong-laser-field coupling to electrons in solid targets with wavelength-scale

spheres", Phys. Rev. Lett. 98(4), 045001 (2007) [DOI]: 10.1103/PhysRevLett.98.045001.

26 V. Floquet, O. Klimo, J. Psikal, A. Velyhan, J. Limpouch, J. Proska, F. Novotny, L. Stolcova, A. Macchi, A. Sgattoni, L. Vassura, L. Labate, F. Baffigi, L. A. Gizzi, P. Martin, and T. Ceccotti, "Micro-sphere layered targets efficiency in laser driven proton acceleration", J. Appl. Phys. 114(8) (2013) [DOI]: 10.1063/1.4819239.

27 H. Habara, A. D. Lad, R. Nagami, P. K. Singh, G. Chatterjee, A. Adak, M. Dalui, J. Jha, P. Brijesh, Y. Mishima, K. Nagai, H. Sakagami, S. Tata, T. M. Trivikram, M. Krishnamurthy, K. A. Tanaka, and G. R. Kumar, "Micro-optics for ultra-intense lasers", A.I.P. Adv. 11(3) (2021) [DOI]: 10.1063/5.0038023..

28 S. P. Gordon, T. Donnelly, A. Sullivan, H. Hamster, and R. W. Falcone, "X rays from microstructured targets heated by femtosecond lasers", Opt. Lett. 19(7), 484-486 (1994) [DOI]: 10.1364/OL.19.000484.

29 J. J. Rocca, M. G. Capeluto, R. Hollinger, S. Wang, Y. Wang, G. R. Kumar, A. D. Lad, A. Pukhov, and V. N. Shlyaptsev, "Ultra-intense femtosecond laser interactions with aligned nanostructures," Optica 11(3), 437-453 (2024) [DOI]: 10.1364/OPTICA.510542

30 M. A. Purvis, V. N. Shlyaptsev, R. Hollinger, C. Bargsten, A. Pukhov, A. Prieto, Y. Wang, B. M. Luther, L. Yin, S. Wang, and J. J. Rocca, "Relativistic plasma nanophotonics for ultrahigh energy density physics", Nat. Photonics 7(10), 796-800 (2013) [DOI]: 10.1038/nphoton.2013.217.

31 C. Bargsten, R. Hollinger, M. G. Capeluto, V. Kaymak, A. Pukhov, S. Wang, A. Rockwood, Y. Wang, D. Keiss, R. Tommasini, R. London, J. Park, M. Busquet, M. Klapisch, V. N. Shlyaptsev, J. J. Rocca, "Energy penetration into arrays of aligned nanowires irradiated with relativistic intensities: Scaling to terabar pressures", Sci. Adv. 3(1), e1601558 (2017) [DOI]: 10.1126/sciadv.1601558.

32 A. Curtis, C. Calvi, J. Tinsley, R. Hollinger, V. Kaymak, A. Pukhov, S. Wang, A. Rockwood, Y. Wang, V. N. Shlyaptsev, and J. J. Rocca, "Micro-scale fusion in dense relativistic nanowire array plasmas", Nat. Commun. 9(1), 1077 (2018) [DOI]: 10.1038/s41467-018-03445-z.

33 A. Curtis, R. Hollinger, C. Calvi, S. Wang, S. Huanyu, Y. Wang, A. Pukhov, V. Kaymak, C. Baumann, J. Tinsley, V. N. Shlyaptsev, and J. J. Rocca, "Ion acceleration and D-D fusion neutron generation in relativistically transparent deuterated nanowire arrays", Phys. Rev. Research 3(4) (2021) [DOI]: 10.1103/PhysRevResearch.3.043181.

34 D. Kong, G. Zhang, Y. Shou, S. Xu, Z. Mei, Z. Cao, Z. Pan, P. Wang, G. Qi, Y. Lou, Z. Ma, H. Lan, W. Wang, Y. Li, P. Rubovic, M. Veselsky, A. Bonasera, J. Zhao, Y. Geng, Y. Zhao, C. Fu, W. Luo, Y. Ma, X. Yan, and W. Ma, "High-energy-density plasma in femtosecond-laser-irradiated nanowire-array targets for nuclear reactions", Matter Radiat. Extremes 7(6) (2022) [DOI]: 10.1063/5.0120845.

35 A. Moreau, R. Hollinger, C. Calvi, S. Wang, Y. Wang, M.G. Capeluto, A. Rockwood, A. Curtis, S. Kasdorf, V.N. Shlyaptsev, V. Kaymak, A. Pukhov, and J.J. Rocca, "Enhanced electron acceleration in

aligned nanowire arrays irradiated at highly relativistic intensities," Plasma Phys Control Fusion 62(1), 014013 (2020). [DOI]: 10.1088/1361-6587/ab4d0c

36 S. Vallières, M. Salvadori, A. Permogorov, G. Cantono, K. Svendsen, Z. Chen, S. Sun, F. Consoli, E. d'Humières, C. G. Wahlström, and P. Antici, "Enhanced laser-driven proton acceleration using nanowire targets", Sci. Rep. 11(1), 2226 (2021) [DOI]: 10.1038/s41598-020-80392-0.

37 R. Hollinger, C. Bargsten, V. N. Shlyaptsev, V. Kaymak, A. Pukhov, M. G. Capeluto, S. Wang, A. Rockwood, Y. Wang, A. Townsend, A. Prieto, P. Stockton, A. Curtis, and J. J. Rocca, "Efficient picosecond x-ray pulse generation from plasmas in the radiation dominated regime", Optica 4(11), 1344 (2017) [DOI]: 10.1364/OPTICA.4.001344.

38 Y. Shou, D. Kong, P. Wang, Z. Mei, Z. Cao, Z. Pan, Y. Li, S. Xu, G. Qi, S. Chen, J. Zhao, Y. Zhao, C. Fu, W. Luo, G. Zhang, X. Yan, and W. Ma, "High-efficiency water-window x-ray generation from nanowire array targets irradiated with femtosecond laser pulses", Opt. Express 29(4), 5427-5436 (2021) [DOI]: 10.1364/OE.417512.

39 J. Park, R. Tommasini, R. Shepherd, R. A. London, C. Bargsten, R. Hollinger, M. G. Capeluto, V. N. Shlyaptsev, M. P. Hill, V. Kaymak, C. Baumann, A. Pukhov, D. Cloyne, R. Costa, J. Hunter, S. Maricle, J. Moody, and J. J. Rocca, "Absolute laser energy absorption measurement of relativistic 0.7-ps laser pulses in nanowire arrays", Phys. Plasmas 28(2) (2021) [DOI]: 10.1063/5.0035174.

40 G. Cristoforetti, P. Londrillo, P. K. Singh, F. Baffigi, G. D'Arrigo, A. D. Lad, R. G. Milazzo, A. Adak, M. Shaikh, D. Sarkar, G. Chatterjee, J. Jha, M. Krishnamurthy, G. R. Kumar, and L. A. Gizzi, "Transition from Coherent to Stochastic electron heating in ultrashort relativistic laser interaction with structured targets", Sci. Rep. 7(1), 1479 (2017) [DOI]: 10.1038/s41598-017-01677-5.

41 D. Tanaka, Y. Maeda, Y. Hironaka, K. Kawasaki, N. Higashi, N. Iwata, Y. Sentoku, R. Kodama, N. Ozaki, T. Somekawa, S. Shinguubara, T. Shimizu, H. Sawada, and K. Shigemori, "Ultrahigh-energy density state in nanowire arrays irradiated with picosecond kilojoule-class ultra-intense laser", A.I.P. Adv. 13(12) (2023) [DOI]: 10.1063/5.0175090.

42 Y. Maeda, Y. Hironaka, T. Iwasaki, K. Kawasaki, Y. Sakawa, T. Izumi, M. Ota, S. Egashira, Y. Nakagawa, N. Higashi, Y. Sentoku, R. Kodama, N. Ozaki, T. Matsuoka, T. Somekawa, T. Yabuuchi, Y. Inubushi, T. Togashi, A. Kon, K. Sueda, K. Miyanishi, S. Shingubara, T. Shimizu, A. Okumura, and K. Shigemori, "Observation of ultra-high energy density state with x-ray free electron laser SACLA", High Energy Density Phys. 36 (2020) [DOI]: 10.1016/j.hedp.2020.100813.

43 O.S. Humphries, P. Allan, C.R.D. Brown, L.M.R. Hobbs, S.F. James, M.G. Ramsay, B. Williams, D.J. Hoarty, M.P. Hill, and S.M. Vinko, "Time evolution of transient plasma states from nanowire arrays irradiated at relativistic intensities," Commun Phys 3(1), (2020). [DOI]: 10.1038/s42005-020-00438-7

44 H. Sawada, T. Yabuuchi, N. Higashi, T. Iwasaki, K. Kawasaki, Y. Maeda, T. Izumi, Y. Nakagawa, K. Shigemori, Y. Sakawa, C. B. Curry, M. Frost, N. Iwata, T. Ogitsu, K. Sueda, T. Togashi, S. H. Glenzer,

A. J. Kemp, Y. Ping, and Y. Sentoku, “Ultrafast time-resolved 2D imaging of laser-driven fast electron transport in solid density matter using an x-ray free electron laser”, Rev. Sci. Instrum. 94(3), 033511 (2023) [DOI]: 10.1063/5.0130953.

45 K. Tono, T. Togashi, Y. Inubushi, T. Sato, T. Katayama, K. Ogawa, H. Ohashi, H. Kimura, S. Takahashi, K. Takeshita, H. Tomizawa, S. Goto, T. Ishikawa, and M. Yabashi, “Beamline, experimental stations and photon beam diagnostics for the hard x-ray free electron laser of SACLA”, New J. Phys. 15(8) (2013) [DOI]: 10.1088/1367-2630/15/8/083035.

46 T. Yabuuchi, A. Kon, Y. Inubushi, T. Togahi, K. Sueda, T. Itoga, K. Nakajima, H. Habara, R. Kodama, H. Tomizawa, and M. Yabashi, “An experimental platform using high-power, high-intensity optical lasers with the hard X-ray free-electron laser at SACLA”, J. Synchrotron Radiat. 26(2), 585-594 (2019) [DOI]: 10.1107/S1600577519000882.

47 A. Zhang, Gengfeng Zheng, and C. M. Lieber, *Nanowires* (Springer, Cham, 2016).

48 S. Shingubara, O. Okino, Y. Sayama, H. Sakaue, T. Takahagi, “Ordered two-dimensional nanowire array formation using self-organized nanoholes of anodically oxidized aluminum”, Jpn. J. Appl. Phys. 36(12S), 7791 (1997) [DOI]: 10.1143/JJAP.36.7791.

49 H. Masuda and K. Fukuda, “Ordered metal nanohole arrays made by a two-step replication of honeycomb structures of anodic alumina”, Science 268(5216), 1466-1468 (1995) [DOI]: 10.1126/science.268.5216.1466.

50 W. Lee and S. J. Park, “Porous anodic aluminum oxide: Anodization and templated synthesis of functional nanostructures”, Chem. Rev. 114(15), 7487-7556 (2014) [DOI]: 10.1021/cr500002z.

51 Y. Liang, C. Zhen, D. Zou, and D. Xu, “Preparation of free-standing nanowire arrays on conductive substrates”, J. Am. Chem. Soc. 126(50), 16338-16339 (2004) [DOI]: 10.1021/ja044545v.

52 L. Xu, Y. Yang, Z.-W. Hu, and S.-H Yu, “Comparison Study on the Stability of Copper Nanowires and Their Oxidation Kinetics in Gas and Liquid”, ACS Nano 10 (3), 3823-3834 (2016), [DOI]: 10.1021/acsnano.6b00704

53 J. Iijima, J.-W. Lim, S.-H. Hong, S. Suzuki, K. Mimura, M. Isshiki, “Native oxidation of ultra high purity Cu bulk and thin films”, Applied Surface Science, 253 (5), 2825-2829 (2006), [DOI]: 10.1016/j.apsusc.2006.05.063.

54 T. Kameshima, A. Takeuchi, K. Uesugi, T. Kudo, Y. Kohmura, K. Tamasaku, K. Muramatsu, T. Yanagitani, M. Yabashi, and T. Hatsui, “Development of an X-ray imaging detector to resolve 200-nm line-and-space patterns by using transparent ceramics layers bonded by solid-state diffusion”, Opt. Lett. 44(6), 1403-1406 (2019) [DOI]: 10.1364/OL.44.001403.

55 B.L. Henke, E.M. Gullikson, and J.C. Davis, “X-Ray Interactions: Photoabsorption, Scattering, Transmission, and Reflection at E = 50-30,000 eV, Z = 1-92,” At Data Nucl Data Tables 54(2), 181–342 (1993) [DOI]: 10.1006/adnd.1993.1013

56 S. B. Hansen, E. C. Harding, P. F. Knapp, M. R. Gomez, T. Nagayama, and J. E. Bailey, “Fluorescence and absorption spectroscopy for warm dense matter studies and ICF plasma diagnostics”, Phys. Plasmas 25(5) (2018) [DOI]: 10.1063/1.5018580.

57 F. Dorchies, F. Festa, V. Recoules, O. Peyrusse, A. Benuzzi-Mounaix, E. Brambrink, A. Levy, A. Ravasio, M. Koenig, T. Hall, and S. Mazevet, “X-ray absorption K edge as a diagnostic of the electronic temperature in warm dense aluminum”, Phys. Rev. B 92(8) (2015) [DOI]: 10.1103/PhysRevB.92.085117.

58 H. Sawada, T. Yabuuchi, N. Higashi, T. Iwasaki, K. Kawasaki, Y. Maeda, T. Izumi, Y. Nakagawa, K. Shigemori, Y. Sakawa, C. B. Curry, M. Frost, N. Iwata, T. Ogitsu, K. Sueda, T. Togashi, S. X. Hu, S. H. Glenzer, A. J. Kemp, Y. Ping & Y. Sentoku “Spatiotemporal dynamics of fast electron heating in solid-density matter via XFEL”, Nat Commun 15, 7528 (2024) [DOI]: 10.1038/s41467-024-51084-4.